First search for r-mode gravitational waves from PSR J0537-6910

Liudmila Fesik[1, 2, a] and Maria Alessandra Papa[1, 2, 3, b]

[1] *Max Planck Institute for Gravitational Physics (Albert Einstein Institute), Callinstrasse 38, 30167 Hannover, Germany*
[2] *Leibniz Universität Hannover, D-30167 Hannover, Germany*
[3] *University of Wisconsin Milwaukee, 3135 N Maryland Ave, Milwaukee, WI 53211, USA*

We report results of the first search to date for continuous gravitational waves from unstable r-modes from the pulsar PSR J0537-6910. We use data from the first two observing runs of the Advanced LIGO network. We find no significant signal candidate and set upper limits on the amplitude of gravitational wave signals, which are within an order of magnitude of the spin-down values. We highlight the importance of having timing information at the time of the gravitational wave observations, i.e. rotation frequency and frequency-derivative values, and glitch occurrence times, such as those that a NICER [1] campaign could provide.

I. INTRODUCTION

Fast spinning neutron stars are among the most promising sources of gravitational radiation. Non-axisymmetric quadrupole deformations and "wobbles" of rotating stars will produce quasi-monochromatic long-lasting gravitational emission – continuous gravitational waves (CWs). In addition, gravitational radiation can destabilize *r-modes* – quasi-normal stellar oscillations of rotating stars [2–4] – and give rise to substantial continuous gravitational wave emission. This instability is particularly interesting in hot young neutron stars because it could provide an effective spin-down mechanism [5].

If neutron stars form in collapse processes, from the conservation of angular momentum one might expect their initial spin to be close to the theoretical maximum that their structure could support, between 500 and 2000 Hz, depending on the equation of state. The observations, however, indicate that young neutron stars present rather smaller spins. Gravitational-wave driven r-mode instabilities have been proposed as a mechanism to explain the missing young fast-rotating pulsars [6].

The fastest and the most energetic known young pulsar is PSR J0537-6910. This object is associated with the supernova remnant N157B in the Large Magellanic Cloud, its age is estimated to be 4000 years and it is spinning at about 62 Hz [7, 8]. This spin frequency may be just below the predicted final frequency for the r-mode emission mechanism [9].

The analysis of 13 years (1999–2011) of X-ray spin timing observations of PSR J0537-6910 with the *Rossi X-ray Timing Explorer* (RXTE) has revealed an extreme glitch activity with abrupt spin-ups (*glitches*) every few months and a subsequent post-glitch relaxation phases [10]. A recent study of the post-relaxation phase data has found an intriguing indication: the average braking index during these periods is ≈ 7.4 [11].

Why is this intriguing? The braking index n is commonly used to describe the spin evolution of neutron stars, $\dot{\nu}(t) \propto \nu(t)^n$, with $n = \nu\ddot{\nu}/\dot{\nu}^2$, with ν indicating the spin frequency. If the star's spin evolution is driven by magnetic dipole emission $n = 3$; if quadrupolar gravitational wave emission is the culprit then $n = 5$; for r-modes $n = 7$. This means that the measured value of the braking index $n \approx 7.4$ is suggestive that unstable r-mode emission might be the main driver of the spin evolution of PSR J0537-6910.

With this background we perform a directed search for continuous gravitational waves from PSR J0537-6910 assuming that the emission stems from unstable r-modes. We use data from the Advanced LIGO network (aLIGO) [12–14] spanning the period between Sept, 2015 and Aug, 2017. Since EM observations of J0537 are not available for this period, the pulsar's rotational parameters are not precisely known and its glitch activity is unknown.

The paper is organized as follows: we summarise relevant results from the timing analysis of EM data in Sec. II. Relations between the expected GW-frequency and spin of the pulsar are defined in Sec. III, followed by the description of the detection method and the search parameter space in Sec. IV C. The results of the search are presented in Sec. V.

II. SPIN EVOLUTION OF J0537-6910

PSR J0537-6910 is spinning at $\approx 62\,\mathrm{Hz}$ with a strong spin-down rate $\dot{\nu} \approx -2\times10^{-10}\,\mathrm{Hz/s}$. Its spin evolution is usually described as the superposition of two trends: the long-term (LT) evolution that describes the spin evolution on the timescale of years and the short-term (ST) evolution that describes the post-glitch recovery phase and is appropriate for weeks after a glitch [10].

The long-term braking index n_{LT} of J0537-6910 is derived by fitting the measurements of $\dot{\nu}$ at the mid-time epochs between two subsequent glitches – glitch-free or *inter-glitch* intervals – over 13 years of data. The result is $n_{\mathrm{LT}} = -1.22$ with a negative second-order frequency derivative $\ddot{\nu}_{\mathrm{LT}} = -7.7\times10^{-22}\,\mathrm{Hz/s^2}$ [10].

The inter-glitch evolution is estimated through a

[a] liudmila.fesik@aei.mpg.de
[b] maria.alessandra.papa@aei.mpg.de

phase-coherent timing analysis of the 45 known post-glitch intervals and yields a wide range of braking indices, with most $n_{\rm ig} > 10$ [10]. A detailed analysis [11] shows that the largest contributions to $n_{\rm ig}$ come from epochs ≤ 50 days after a glitch, indicating the existence of an early fast relaxation phase. In contrast, an asymptotic value of $n_{\rm ig}$ for the longer time intervals is ≈ 7.4 (Fig. 3 in [11]), which might reflect the fact that gravitational wave emission due to r-mode instability is causing the observed spin-down. For simplicity we will assume that r-mode emission sets-in 50 days after a glitch.

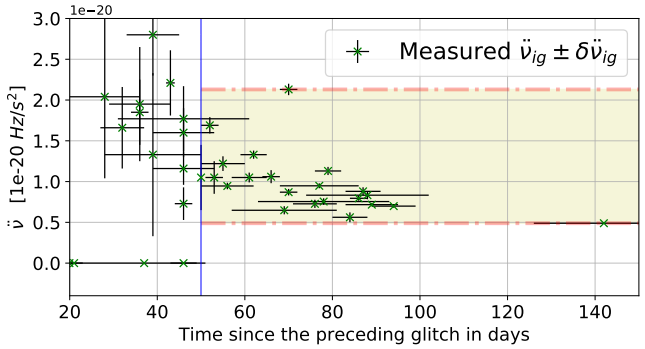

FIG. 1: Distribution of measured $\ddot{\nu}_{\rm ig} \pm \delta\ddot{\nu}_{\rm ig}$ for every known inter-glitch period, as a function of the fit epoch. The fit epochs is 0 at the time of each glitch. (We used the data from Tab. 1 of [10].)

.

Fig. 1 shows the second-order frequency derivative values for the various inter-glitch periods as a function of the epoch of the measurement. For epochs which are more than 50 days after the glitch, $\ddot{\nu}_{\rm ig} \in [4.89(7)\times 10^{-21}, 2.13(7)\times 10^{-20}]$ Hz/s^2, Tab. 1 of [10].

The most important values from the timing analysis of PSR J0537-6910 are summarised in Tab. I.

Sky position			
α [rad]	0.09825990	δ [rad]	-1.20728496
Long-term evolution			
$n_{\rm LT}$	-1.22 ± 0.04	$\ddot{\nu}_{\rm LT}$ [Hz/s^2]	$-7.7\times10^{-22} \pm 3\times10^{-23}$
Short-term evolution			
$n_{\rm ig}$	7.4 ± 0.7	$\ddot{\nu}_{\rm ig}^{\rm min}$ [Hz/s^2]	$4.89\times10^{-21} \pm 7\times10^{-23}$
		$\ddot{\nu}_{\rm ig}^{\rm max}$ [Hz/s^2]	$2.13\times10^{-20} \pm 7\times10^{-22}$
The last observation			
fit epoch $t_{\rm obs}$ [GPS]		1004659215	
$\nu\|_{t_{\rm obs}}$ [Hz]		$61.961105096 \pm 5 \times 10^{-9}$	

TABLE I: Evolution parameters of PSR J0537-6910 [10]

III. GW-EMISSION FROM R-MODES

The strongest gravitational waves are expected from the quadrupole ($l = m = 2$) r-mode, so we concentrate on this. The gravitational wave frequency f associated with this mode depends on the neutron star structure and its rotation frequency ν in a non-trivial manner [4, 5]. We follow the prescription of [15] and use the following relations:

$$\begin{cases} f/\nu = A - B\,(\nu/\nu_{\rm K})^2 \\ \dot{f}/\dot{\nu} = A - 3B\,(\nu/\nu_{\rm K})^2 \\ \ddot{f}/\ddot{\nu} = A - 3B\,(\nu/\nu_{\rm K})^2\left(1 - \frac{2}{n}\right) \end{cases} \quad (1)$$

with n being the braking index during the r-mode phase, $\nu_{\rm K}$ the Kepler frequency of the star, and the quantities $1.39 \leq A \leq 1.57$ and $0 \leq B \leq 0.195$ encoding information on the neutron star structure. Based on the observed highest spin frequency of pulsars at 716 Hz, following [15], we take $\nu_{\rm K} = 506$ Hz as a *conservative estimate*.

The uncertainties in the values of A and B give rise to ranges of values for the gravitational wave frequency and frequency derivatives. Since A is always $\gg 3B(\nu/\nu_{\rm K})^2$ they take the form:

$$\begin{cases} \left(1.39 - 0.195\ \frac{\nu^2}{\nu_{\rm K}^2}\ \right) \nu \leq f \leq 1.57\ \nu \\ \left(1.39 - 0.585\ \frac{\nu^2}{\nu_{\rm K}^2}\ \right) |\dot{\nu}| \leq |\dot{f}| \leq 1.57\ |\dot{\nu}| \\ \left(1.39 - 0.585\ \frac{\nu^2}{\nu_{\rm K}^2}\ \right) \left(1 - \frac{2}{7}\right)\ \ddot{\nu} \leq \ddot{f} \leq 1.57\ \ddot{\nu} \end{cases} \quad (2)$$

and we note that $\dot{\nu} = -|\dot{\nu}|$ and $\dot{f} = -|\dot{f}|$.

IV. THE GRAVITATIONAL WAVE SEARCH

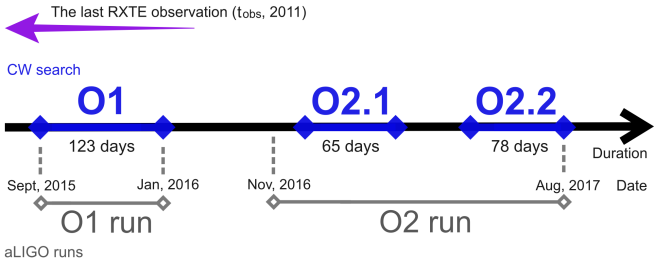

FIG. 2: The data from O1 and O2 aLIGO observing runs used for CW searches.

.

A. The data input

We use the data from the two Advanced LIGO (aLIGO) detectors located in Hanford (WA) and Livingston (LA), USA [16]. We search the publicly available data from the first two observing runs O1 and O2 [12–14]. O1 took place between September 12, 2015 and January

19, 2016 and covered about 4 months of data [17, 18]. The second run (O2) operated from November 30, 2016 to August 25, 2017 and includes a significant gap in the data between March 15th and June 8th 2017 [19, 20]. This gap naturally provides two stretches of contiguous data, which we consider as two independent time baselines for our searches: *O2.1* and *O2.2*, as shown in Fig. 2.

The search input consists of Short time-baseline Fourier transforms (SFTs) [21], from data segments 1800 s long. Instrumental and environmental spectral disturbances are removed to avoid contamination of the results, as done in previous searches [22, 23].

B. The signal waveform

The signal at each detector, $h(t)$, is a superposition of the two polarization waveforms $h_+(t)$ and $h_\times(t)$

$$h(t) = F_+(\alpha,\delta,\psi;t)h_+(t) + F_\times(\alpha,\delta,\psi;t)h_\times(t), \quad (3)$$

where $F_+(\alpha,\delta,\psi;t)$ and $F_\times(\alpha,\delta,\psi;t)$ are the detector beam pattern functions and

$$\begin{aligned} h_+(t) &= A_+ \cos\Phi(t) \\ h_\times(t) &= A_\times \sin\Phi(t). \end{aligned} \quad (4)$$

If ι is the angle between the total angular momentum of the star and the direction from the star to Earth

$$\begin{aligned} A_+ &= \frac{1}{2}h_0(1+\cos^2\iota) \\ A_\times &= h_0\cos\iota. \end{aligned} \quad (5)$$

h_0 is the intrinsic gravitational wave amplitude, (α,δ) are the right-ascension and declination for the source and ψ is the orientation of the wave-frame with respect to the detector frame. Due to Earth's motion, the orientation between the detector and the source is changing all the time, which makes $F_{+,\times}$ time-varying. $\Phi(t)$ is the phase of the gravitational wave signal at time t. If with τ we indicate the arrival time of the wave with phase $\Phi(t)$ at the solar system barycenter (SSB), then

$$\Phi(\tau) = \Phi_0 + 2\pi[f(\tau-\tau_{\rm ref}) + \frac{1}{2}\dot{f}(\tau-\tau_{\rm ref})^2 + \frac{1}{6}\ddot{f}(\tau-\tau_{\rm ref}{}^3 + \cdots]. \quad (6)$$

If the frequency derivatives are non-zero, the reference time $\tau_{\rm ref}$ (or $t_{\rm ref}$) determines the frequency scale. The transformation between detector time t and solar-system-barycenter time τ is

$$\tau(t) = t + \frac{\mathbf{r}(t)\cdot\mathbf{n}}{c} + \Delta_{\rm E\odot} - \Delta_{\rm S\odot}\,, \quad (7)$$

where $\mathbf{r}(t)$ is the position vector of the detector in the SSB frame, $\mathbf{n}$ is the unit vector pointing to the source, and c is the speed of light; $\Delta_{\rm E\odot}$ and $\Delta_{\rm S\odot}$ are respectively the relativistic Einstein and Shapiro time delays. We refer the reader to [24] for further details.

C. The signal-parameter ranges

The position of PSR J0537-6910 is known with high accuracy, so if we knew precisely its spin frequency ν and its derivatives $\dot{\nu},\ddot{\nu}$, from Eq. (2) we could determine the range of possible values of the r-mode gravitational wave frequency f and its derivatives $\dot{f},\ddot{f}$. However, since there are no timing data available for the O1 and O2 data period [10], $\nu,\dot{\nu},\ddot{\nu}$ are not known precisely.

For each search we set the reference time $t_{\rm ref}$ in the middle of each observation period. At that reference time we determine the range of values for $\nu\in[\nu_{\rm min},\nu_{\rm max}]$, $\dot{\nu}\in[\dot{\nu}_{\rm min},\dot{\nu}_{\rm max}]$ and $\ddot{\nu}\in[\ddot{\nu}_{\rm min},\ddot{\nu}_{\rm max}]$. From Eq. 2 the corresponding gravitational wave frequency and derivatives ranges are then

$$\begin{cases} \left(1.39 - 0.195\ \frac{\nu^2}{\nu_{\rm K}^2}\ \right)\Big|_{\nu_{\rm min}} \nu_{\rm min} \le f \le 1.57\ \nu_{\rm max} \\ \left(1.39 - 0.585\ \frac{\nu^2}{\nu_{\rm K}^2}\ \right)\Big|_{\nu_{\rm max}} |\dot{\nu}|_{\rm min} \le |\dot{f}| \le 1.57\ |\dot{\nu}|_{\rm max} \\ \left(0.9929 - 0.4179\ \frac{\nu^2}{\nu_{\rm K}^2}\ \right)\Big|_{\nu_{\rm max}} \ddot{\nu}_{\rm min} \le \ddot{f} \le 1.57\ \ddot{\nu}_{\rm max} \end{cases} \quad (8)$$

The uncertainty in the $\nu,\dot{\nu}$ parameters stems from our ignorance on when glitches occurred, bracketing the gravitational wave observations. If we assume that there is r-mode emission throughout our observation periods, then the spin state of the star at each $t_{\rm ref}$ only depends on how long before $t_{\rm ref}$, the previous glitch happened. We consider two extremes: 1) r-mode emission sets-in just at the beginning of our observation period and lasts for a very long time; 2) r-mode emission sets-in a long time before the beginning of our observations and ends at the end of the observation period, Fig. (3).

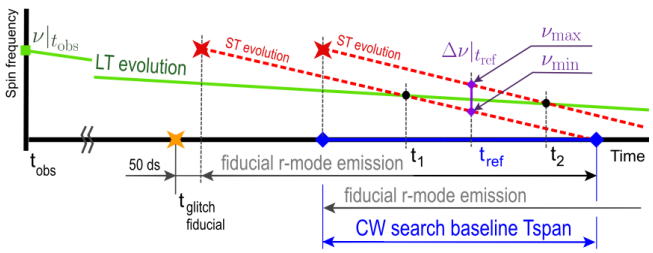

FIG. 3: Spin evolution of the PSR J0537-6910 under the two different scenarios discussed in the text.

How long is the longest time that we can reasonably consider ? We take the longest known inter-glitch period, ≈ 284 days, and imagine that for scenario 1) r-mode emission starts with our observations and lasts $(284-50)$ days, at which time the next glitch happens; for scenario 2) r-mode emission starts $(284-50-T_{\rm span})$ days before the beginning of the observation period (where $T_{\rm span}$ is the duration of the gravitational wave observation in days). In these two cases the inter-glitch epochs, i.e. the mid-

times in-between two successive glitches, are

$$\begin{cases} t_1 = t_0^{\rm gw} + 92 \text{ days} \\ t_2 = t_0^{\rm gw} + T_{\rm span} - 142 \text{ days}, \end{cases} \quad (9)$$

with $t_0^{\rm gw}$ being the time corresponding to the start of the gravitational wave observation period and the subscripts "1" and "2" indicating the two different scenarios. Consistently with [10] we can then determine the signal parameters at t_1 and t_2 by evolving the values of Tab. I defined at the last observed inter-glitch epoch $t_{\rm obs}$ with $n_{\rm LT}, \ddot{\nu}_{\rm LT}$. We obtain $\nu|_{t_1}^{\rm LT}$ and $\nu|_{t_2}^{\rm LT}$. Since $\nu|_{t_1}^{\rm ST} \equiv \nu|_{t_1}^{\rm LT}$, $\nu|_{t_2}^{\rm ST} \equiv \nu|_{t_2}^{\rm LT}$, we use these values to derive the ones at the reference time for each search $t_{\rm ref} = t_0^{\rm gw} + \frac{1}{2}T_{\rm span}$, by evolving them according to the short term (ST) evolution model of Tab. I. Specifically, we consider $n_{\rm ig}$, $\ddot{\nu}_{\rm ig}^{\rm min}$ and $\ddot{\nu}_{\rm ig}^{\rm max}$ and from these, using the definition of braking index, we derive $\dot{\nu}(t_1, n_{\rm ig}, \ddot{\nu}_{\rm ig}^{\rm min})$, $\dot{\nu}(t_2, n_{\rm ig}, \ddot{\nu}_{\rm ig}^{\rm min})$, $\dot{\nu}(t_1, n_{\rm ig}, \ddot{\nu}_{\rm ig}^{\rm max})$ and $\dot{\nu}(t_2, n_{\rm ig}, \ddot{\nu}_{\rm ig}^{\rm max})$. We evolve these to $t_{\rm ref}$ and find four values of $\nu(t_{\rm ref})$ and four values of $\dot{\nu}(t_{\rm ref})$, corresponding to $(t_1, \ddot{\nu}_{\rm ig}^{\rm min})$, $(t_2, \ddot{\nu}_{\rm ig}^{\rm min})$, $(t_1, \ddot{\nu}_{\rm ig}^{\rm max})$ and $(t_2, \ddot{\nu}_{\rm ig}^{\rm max})$. We take $\nu_{\rm min}$, $\nu_{\rm max}$, $\dot{\nu}_{\rm min}$ and $\dot{\nu}_{\rm max}$ as the smallest and largest among the four. These quantities define the range of possible spin frequencies and derivatives. We assume that $\ddot{\nu}_{\rm min} = \ddot{\nu}_{\rm ig}^{\rm min}$ and $\ddot{\nu}_{\rm max} = \ddot{\nu}_{\rm ig}^{\rm max}$.

The reference times for each observation period O1, O2.1 and O2.2 are given in Table IV and the corresponding boundaries for the spin frequency and spindown in Table II:

Search run	O1	O2.1	O2.2
$\nu_{\rm min}$ [Hz]	61.9344(6)	61.9261(8)	61.9236(9)
$\nu_{\rm max}$ [Hz]	61.9365(7)	61.9294(9)	61.9266(9)
$\dot{\nu}_{\rm min}$ [Hz/s]	$-4.22(21)\times10^{-10}$		
$\dot{\nu}_{\rm max}$ [Hz/s]	$-2.02(10)\times10^{-10}$		
$\ddot{\nu}_{\rm min}$ [Hz/s^2]	$4.89(7)\times10^{-21}$		
$\ddot{\nu}_{\rm max}$ [Hz/s^2]	$2.13(7)\times10^{-20}$		

TABLE II: The range of spin frequency and frequency-derivatives for PSR J0537-6910 at the reference time of each search. The parameter uncertainties from Table I are propagated throughout the derivations described in the text and are indicated with brackets.

All these values can be substituted in Eq. (8) and finally yield the gravitational wave frequency and frequency derivative search ranges shown in Table III.

D. Detection statistics

We perform a fully coherent, multi-detector search using a maximum likelihood matched filtering method known as $\mathcal{F}$-statistic [25]. The $\mathcal{F}$-statistic is the optimal frequentist statistic for this type of signal, in the presence of stationary, Gaussian detector noise. The resulting detection values, $2\mathcal{F}$, for each template represent the likelihood that a signal with the template's waveform be present in the data, with respect to Gaussian noise. In Gaussian noise $2\mathcal{F}$ follows a χ^2-distribution with 4 degrees of freedom (χ^2_4) and a non-centrality parameter that equals the squared signal-to-noise ratio, [24].

In the presence of spectral disturbances in the data, the detection statistic can be improved by extending the noise model to include "noise lines", on top of Gaussian noise [26]. The corresponding line-robust statistic $\hat{B}_{\rm SGL}$ requires the choice of the tuning parameter $\mathcal{F}_*^{(0)}$ that defines the single-detector $\mathcal{F}$-statistic magnitude at which $\hat{B}_{\rm SGL}$ begins to down-rank search results with respect to the pure Gaussian noise model. $\mathcal{F}_*^{(0)}$ is usually defined in terms of a Gaussian-noise false-alarm probability $\chi^2(2\mathcal{F}_*^{(0)}|0)$, which we choose to be $\approx 1/N^{\rm eff}$, the effective number of independent templates. The results of the search are ranked according to $\hat{B}_{\rm SGL}$. For this search we estimate that $N^{\rm eff} = 0.9\, N_{\rm tot}$, where $N_{\rm tot}$ is the total number of searched templates.

Search run	O1	O2.1	O2.2
$f_{\rm min}$ [Hz]	85.9078(9)	85.8964(11)	85.8929(12)
$f_{\rm max}$ [Hz]	97.2403(10)	97.2291(14)	97.2247(15)
Δf [Hz]	11.3325(13)	11.3327(18)	11.3318(19)
$\dot{f}_{\rm min}$ [Hz/s]	$-6.63(33)\times10^{-10}$		
$\dot{f}_{\rm max}$ [Hz/s]	$-2.79(13)\times10^{-10}$		
$\Delta\dot{f}$ [Hz/s]	$3.8(4)\times10^{-10}$		
$\ddot{f}_{\rm min}$ [Hz/s^2]	$4.82(7)\times10^{-21}$		
$\ddot{f}_{\rm max}$ [Hz/s^2]	$3.34(11)\times10^{-20}$		
$\Delta\ddot{f}$ [Hz/s^2]	$2.86(11)\times10^{-20}$		

TABLE III: The search parameter space. The brackets indicate uncertainties.

E. The search set up

The search targets different wave shapes, each defined by a value of the gravitational wave frequency and frequency-derivatives, $f, \dot{f}, \ddot{f}$. The ensemble of waveforms obtained by varying the values for the $f, \dot{f}, \ddot{f}$ within the boundaries given by Table III , constitutes the signal template bank of our search.

The grid spacings ($\delta f, \delta\dot{f}, \delta\ddot{f}$) are such that the average loss in detection efficiency due to signal-template mismatch is about 6%. The mismatch distribution is shown Fig. 4. The details of the procedure can for instance be found in [27]. Since the $\delta\ddot{f}$ spacing is smaller than $\ddot{f}_{\rm min}$

Search run	O1	O2.1	O2.2
t_0^{gw} [GPS]	1126623625	1167983370	1180975619
t_{ref} [GPS]	1131937856	1170799164	1184354596
T_{span} [days]	123.2	65.2	78.2
T_{data} [N_{SFT}]	6287	4107	4790
δf [Hz]	3.05×10^{-08}	5.77×10^{-08}	4.80×10^{-08}
$\delta \dot{f}$ [Hz/s]	2.22×10^{-14}	7.92×10^{-14}	5.50×10^{-14}
$\delta \ddot{f}$ [Hz/s^2]	9.89×10^{-21}	6.65×10^{-21}	3.85×10^{-21}
$\log_{10} N^{\mathrm{eff}}$	13.30	12.0	12.23
$\mathcal{F}_*^{(0)}$	32.98	29.89	30.43

TABLE IV: Parameters of each search, including the template grid spacings, the start and reference times t_0^{gw} and t_{ref}, the search time-baseline T_{span}, the total time for which there is data from both detectors T_{data} (expressed as the total number of input SFTs), an estimate of the number of independent templates N^{eff} and the tuning parameter $\mathcal{F}_*^{(0)}$.

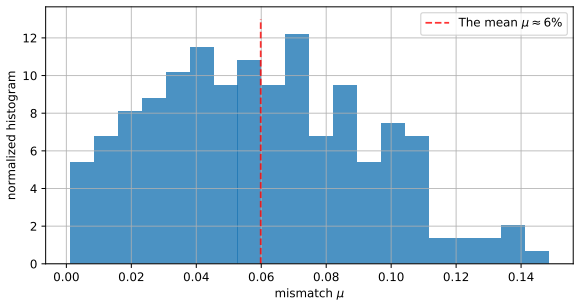

FIG. 4: The mismatch distribution μ for the search template grid computed from 200 searches on fake signals. $\mu = \frac{\rho^2_{\mathrm{PM}} - \rho^2_{\mathrm{grid}}}{\rho^2_{\mathrm{PM}}}$ with ρ^2 being the signal-to-noise measured with a perfect match between signal and template ("PM") and with a search over the original search grid ("grid").

from Eq.s 8, we set $\ddot{f}_{\mathrm{min}} = 0$.

A summary of all search parameters is given in Table IV. Overall, we search $\approx 10^{13}$ templates in every search.

V. RESULTS

Fig. 5 shows the $2\mathcal{F}$ values of the most significant $\hat{B}_{\mathrm{SGL}}$ results in every 0.014 Hz band, after having excluded results close to spectral artefacts that were cleaned-out in the input data [22, 23]. The cleaning procedure substitutes the real data with fake Gaussian noise, hence these data do not contribute any astrophysical information to the results. The extent of the excluded region

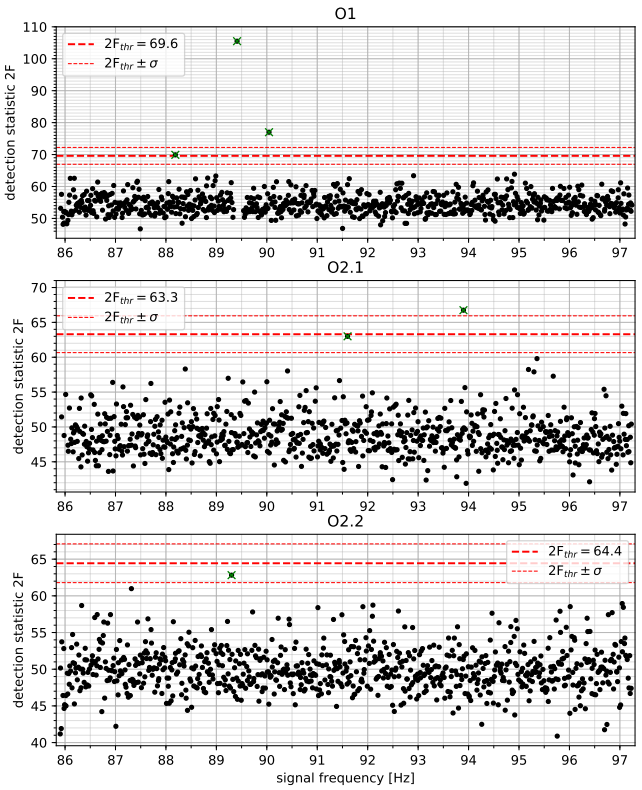

FIG. 5: The most significant candidate in every 0.014 Hz band. We note the value of $2\mathcal{F}_{\mathrm{thr}}$ for each search, the expected highest detection statistic value in Gaussian noise over the number of independent templates searched.

is determined by the extent of the original spectral contamination and by an evaluation of the spread that this would generate in signal-frequency space, for our specific target and for the largest searched $|\dot{f}|$. This removes 2.25% (O1), 1.1% (O2.1) and 3% (O2.2) of the results. The complete list of the bands excluded from further inspection and from the upper limit statements, is given in appendix A.

We compare the $2\mathcal{F}$ values with $2\mathcal{F}_{\mathrm{thr}}$, the expected most significant $2\mathcal{F}$ over the entire search in Gaussian noise:

$$2\mathcal{F}_{\mathrm{thr}} = \int_0^\infty \chi_4^2 \; N^{\mathrm{eff}} \; F_{\chi_4^2}^{(N^{\mathrm{eff}}-1)} \; p_{\chi_4^2} \; d\chi_4^2, \qquad (10)$$

where $p_{\chi_4^2}$ is the probability density function of a χ_4^2 variable and $F_{\chi_4^2}$ its cumulative distribution. We do not use $2\mathcal{F}_{\mathrm{thr}}$ as a rigorous measure of significance but rather as an indicator.

If a candidate were found well above $2\mathcal{F}_{\mathrm{thr}}$ with consistent parameters across the three searches, this would *not* automatically mean that it is a signal from J0537-6910 , but it would certainly warrant further investigation. On the other hand, if no consistent candidate exists above the expected loudest, it is unlikely that we can confi-

dently identify a signal with this search.

f [Hz]	$\dot{f}$ [Hz/s]	$2\mathcal{F}$	$\frac{2\mathcal{F}-2\mathcal{F}_{\rm thr}}{\sigma}$	$\hat{B}_{\rm SGL}$
O1				
89.410489097	-5.096×10^{-10}	105.50	13.65	8.06
90.044112991	-3.753×10^{-10}	77.0	2.85	2.7
88.186443235	-3.476×10^{-10}	69.91	0.16	1.16
O2.1				
93.898823869	-5.358×10^{-10}	66.75	0.88	1.82 $\times$
91.600806439	-3.167×10^{-10}	63.00	-0.55	1.00
O2.2				
89.301450860	-6.071×10^{-10}	62.82	-0.61	0.73

TABLE V: The most significant candidates from each of the searches.

We find 6 candidates with $2\mathcal{F} \geq 2\mathcal{F}_{\rm thr} - \sigma$, and they are listed in Tab. V. We comment only on the three that are at least at the 1σ level.

O1 search: The only overall-outstanding candidate comes from this search, at $\sim$ 89.4 Hz, with a $2\mathcal{F}$ value which is over 13σ of the expected loudest. It however cannot be reasonably ascribed to J0537-6910 because this result comes from a frequency region that is rather disturbed. In order to inspect a broader range of templates we mine the results of an all-sky search on the same data [23]. We recognise that this candidate is indeed one of many having an enhanced value of the detection statistic and with a morphology in parameter space which is typical of disturbances rather than signals.

On very similar grounds we dismiss the candidate at $\sim$ 90.4 Hz. There is no obvious disturbance associated with the third candidate, at $\sim$ 88.2 Hz, its detection statistic is well within the expected amplitude for the loudest and so it is most likely a noise fluctuation. Fig.s 7 illustrate our findings.

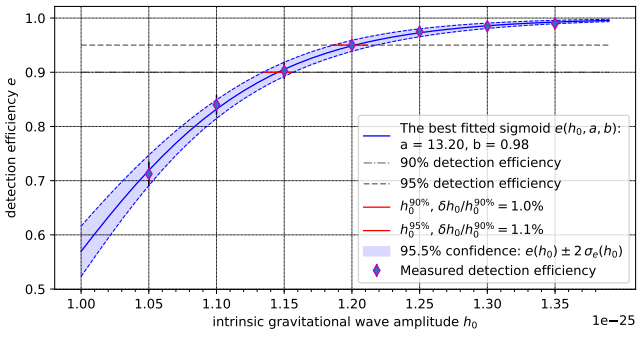

FIG. 6: Detection efficiency curve for the band 87.75 − 88.25 Hz in O2.1 search run.

O2.1 and O2.2 searches: There are no significant candidates from these searches. The candidate at $\sim$ 93.9 Hz is less than 2σ above the expectation and in this frequency range in the O2 data there are more significant candidates at different sky locations.

The candidate at $\sim$ 91.6 Hz appears to be due to a noise fluctuation.

A. Upper limits on the GW amplitude

We set upper limits on the intrinsic gravitational amplitude h_0 in 0.5 Hz bands, based on the highest detection statistic value measured in each band, after the results from the fake Gaussian noise bands are removed. We perform 400 fake-signal search-and-recovery Monte Carlos within each band. The signals are all at the location of J0537-6910 , with frequency, spindown and initial phase values taken from uniform random distributions in their respective ranges. We add these signals in the real data. We consider 6 values of h_0 ranging from 1.05×10^{-25} to 1.35×10^{-25}.

The searches are performed with the same grids and set-up as the search, Tab. III, in the neighbourhood of the fake signal parameters. A signal is counted as recovered if the highest detection statistic value from the fake-signal search is higher than the one recorded in the actual search. The detection efficiency $e(h_0)$ is the fraction of recovered signals.

We adopt a sigmoid of the form $e(h_0) = (1 + \exp(\frac{a-h_0}{b})^{-1}$ to fit h_0 with the corresponding measured detection efficiency. We use Python's "curve fit" package [28] based on the Levenberg-Marquardt algorithm through the least squares method. The uncertainties in e stemming from the measurement error on the number of recovered signals are translated in uncertainties on the fit parameters δa and δb, computed as the square root of the diagonal elements of the covariance matrix. We use δa and δb to estimate the standard deviation $\sigma_e(h_0)$ of the best fit sigmoid $e(h_0)$. Fig. 6 shows an example of the sigmoid fit with two curves $e(h_0) \pm 2\,\sigma_e(h_0)$ that bracket the expected $e(h_0)$ curve with $> 95\%$ confidence.

The 90% confidence upper limit on the intrinsic gravitational wave amplitude is the smallest h_0 such that 90% of the target signal population in the search range would have produced a value of the detection statistic higher than the one that was measured in the search. We read this value, $h_0^{90\%}$, off the sigmoid fit curve at $e = 0.9$.

The uncertainty δe determines the range of variability for $h_0^{90\%}$ which overall amounts to $\leq 2\%$ of the upper limit value. We add the calibration uncertainty which we conservatively take to be 5% [29]. The upper limits together with their uncertainties are plotted in Fig. 8 for all 3 search runs. They are provided in tabular form in the appendix B and in machine-readable format at [30]. We also compute the 95% confidence upper limits, which are $\approx 3.9\%$ higher than the 90% confidence ones.

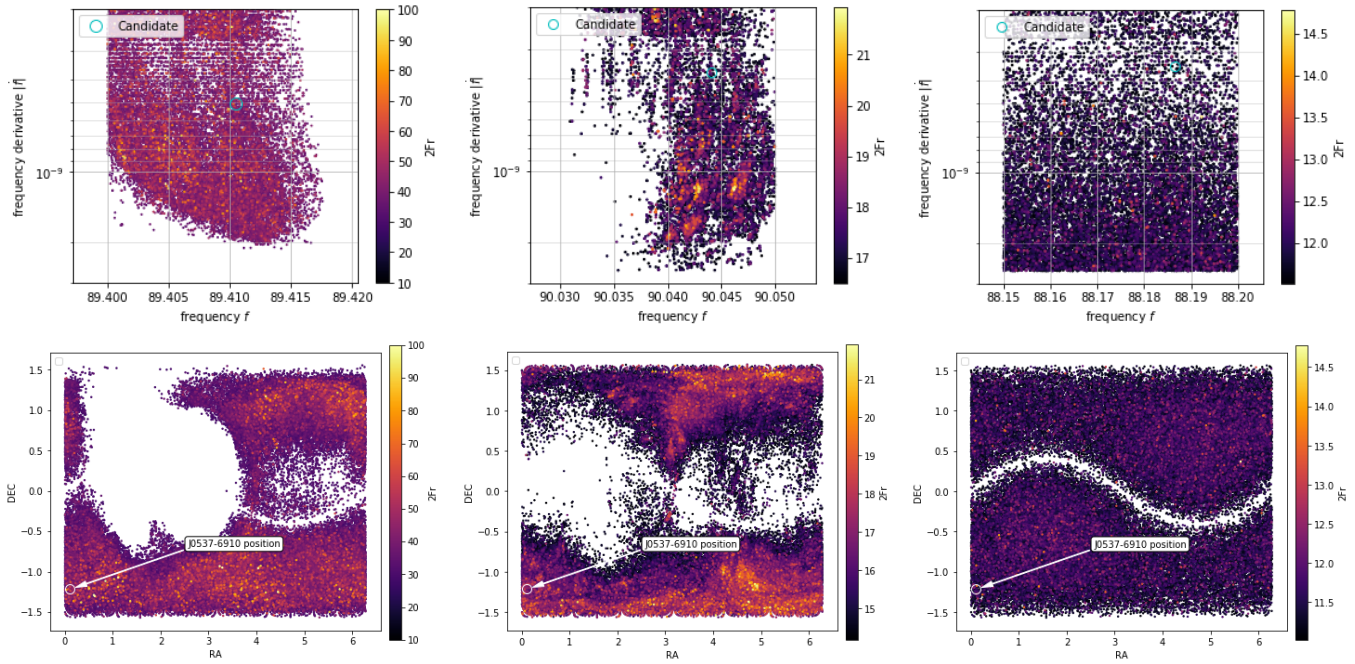

(a) Candidate 1 at $f = 89.41\,\mathrm{Hz}$ (b) Candidate 2 at $f = 90.0\,\mathrm{Hz}$ (c) Candidate 3 at $f = 88.18\,\mathrm{Hz}$

FIG. 7: Results of the all-sky O1 search [23] in the parameter regions of the three O1 candidates of Table V. The plots show the detection statistic values (color-coded) as a function of the template waveform frequency and frequency derivative in the top panels, and as a function of source position (α, δ) in the bottom panels. When a spectral region is contaminated, the distribution of candidates is not uniform in parameter space, and this can be clearly seen in panels (a) and (b), as opposed to panel (c) that portrays results from an undisturbed frequency region.

1. *Sensitivity depth*

The sensitivity depth is a useful measure to compare the baseline performance of different searches [31]. It was first introduced in [27] as

$$\mathcal{D}^{90\%}(f) = \frac{\sqrt{S_h(f)}}{h_0^{90\%}(f)} \quad [1/\sqrt{\mathrm{Hz}}], \tag{11}$$

where $\sqrt{S_h(f)}$ is the noise level associated with the signal frequency f. The multi-detector $S_h(f)$ for our searches is the harmonic mean of the single-detector power spectral densities S_h^H and S_h^L of the data, then averaged over the 0.5 Hz frequency band that the upper limit value refers to. The resulting $\mathcal{D}^{90\%}(f)$ is shown in Fig. 9 and tabulated in Appendix B. We provide the values of $S_h(f)$ in machine readable format at [30].

2. *Spin-down limit*

If all the kinetic energy lost by J0537-6910 (its spin-down) rotating at ν is due to gravitational emission at frequency f, its gravitational wave amplitude is

$$h_0^{\mathrm{sd}} = \frac{1}{D}\sqrt{\frac{10G}{c^3} I_{zz} \frac{|\dot{\nu}|\nu}{f^2}} \tag{12}$$

where I_{zz} is the moment of inertia of the star with spin axis in the $\hat{z}$ direction. If in Eq.s 1 we neglect the terms in $(\nu/\nu_{\mathrm{K}})^2$ (slowly rotating star) and set $A = f/\nu$ then

$$h_0^{\mathrm{sd}} = \frac{1}{A\,D}\sqrt{\frac{10G}{c^3} I_{zz} \frac{|\dot{\nu}|}{\nu}}. \tag{13}$$

This is a general formula that applies to any emission mechanism. If the emission is due to an equatorial ellipticity in the star, then $A = 2$ and we find the commonly-seen spindown-limit formula, for example Eq. 5 of [32].

In the case of r-mode emission A encodes information on the equation of state of the star. As shown in Fig. 10, mass M and radius R are different functions of A for different equations of state. If $\mathcal{C} = M/R$ is the compactness of the star, then $A = |-1.373 + .079\,\mathcal{C} - 2.25\,\mathcal{C}^2| \in [1.39; 1.57]$ for $M \in [1.02 - 2.76\,M_\odot]$ and compactness $\mathcal{C} = M/R \in [0.11, 0.31]$. This was found by fitting 14 realistic equations of state by [33] and we will use it in Eq. 14 to compute $M(A)$ and $R(A)$ from $M(\mathcal{C})$ and $R(\mathcal{C})$ given in [34, 35].

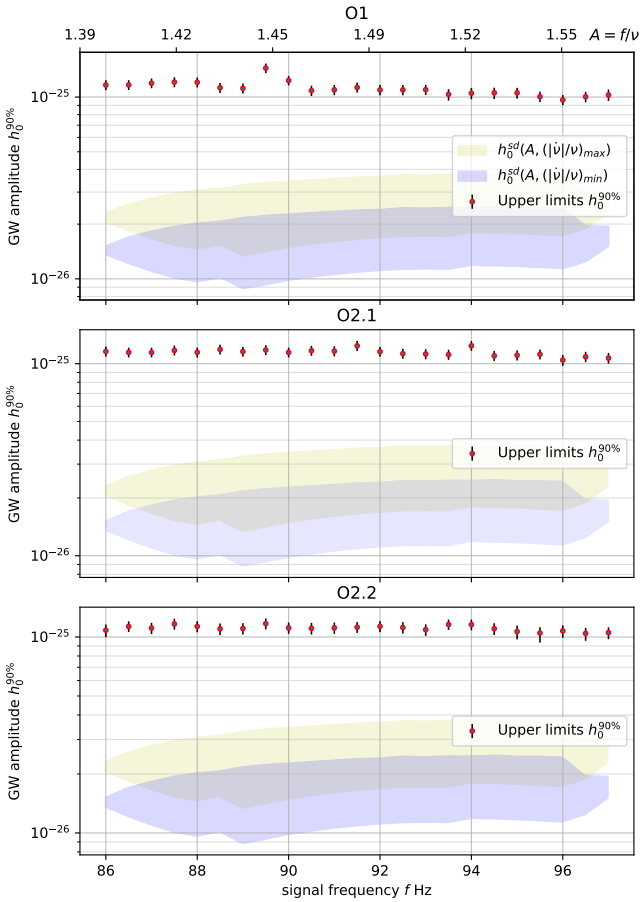

FIG. 8: The markers show the upper limits on GW amplitude $h_0^{90\%}$ for a continuous signal from J0537-6910 from each of the searches.The shaded regions show the range of values that the spin-down upper limit could take, depending on the equation of state of the the star, as described in Section V A 2. The second x-axis, on the top, shows $A(f)$ for the $h_0^{\mathrm{sd}^{\max}}$ curve, i.e. $A = f/\nu_{\min}$. On this scale it is however not possible to appreciate the difference with $A = f/\nu_{\max}$, so the plotted axes hold for all quantities shown.

The moment of inertia I_{zz} also depends on the equation of state. We re-write it in terms of the normalized moment of inertia $\bar{I} := I_{zz}/M^3$ that can be expressed in terms of $\mathcal{C}$ for slowly rotating stars with the coefficients given in Tab. 2 of [36].

Eq. (13) then becomes

$$h_0^{\mathrm{sd}}(A, \frac{|\dot{\nu}|}{\nu}) = \frac{1}{A\,D}\sqrt{\frac{10G}{c^3}\bar{I}(A)M^3(A)\frac{|\dot{\nu}|}{\nu}}. \qquad (14)$$

We consider two extremes:

$$\begin{cases} h_0^{\mathrm{sd}^{\min}}(A) = h_0^{\mathrm{sd}}(A, \frac{|\dot{\nu}|}{\nu}|_{\min}), & \frac{|\dot{\nu}|}{\nu}|_{\min} = |\dot{\nu}|_{\min}/\nu_{\max} \\ h_0^{\mathrm{sd}^{\max}}(A) = h_0^{\mathrm{sd}}(A, \frac{|\dot{\nu}|}{\nu}|_{\max}), & \frac{|\dot{\nu}|}{\nu}|_{\max} = |\dot{\nu}|_{\max}/\nu_{\min}. \end{cases} \qquad (15)$$

As $M(A)$ varies in the range shown in middle panel

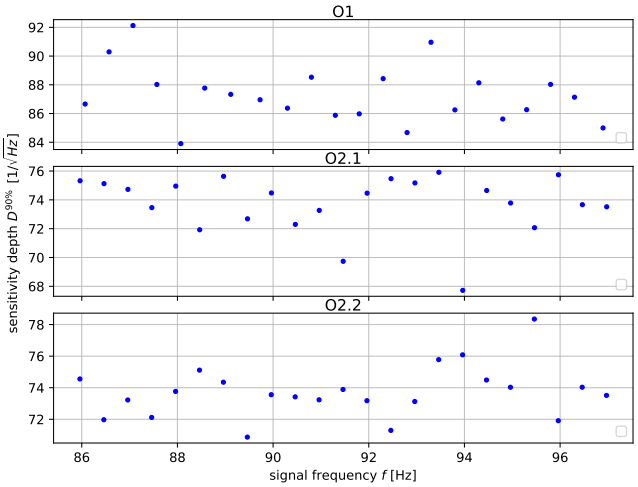

FIG. 9: The sensitivity depth

of Fig. 10, we find the corresponding range $\Delta h_0^{\mathrm{sd}^{\min}}$ and $\Delta h_0^{\mathrm{sd}^{\max}}$. We set $A = f/\nu_{\min}$ in $\Delta h_0^{\mathrm{sd}^{\max}}$ and $A = f/\nu_{\max}$ in $\Delta h_0^{\mathrm{sd}^{\min}}$ and derive the two differently shaded regions of Fig. 8 which define range of variability of the spin-down upper limit h_0^{sd}. We are neglecting the $B\nu^2/\nu_{\mathrm{K}}^2$ term of Eq. 1 for simplicity. This approximation is completely unimportant in the context of sketching the boundaries of h_0^{sd}.

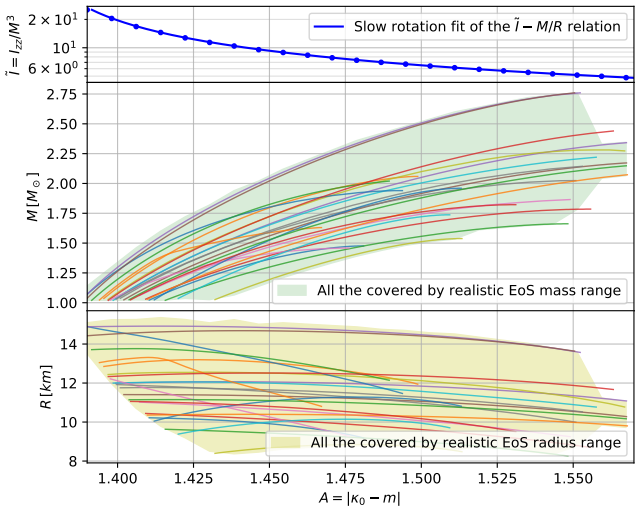

FIG. 10: $\tilde{I} - M/R$ Universal relation and ranges of M and R from realistic EoS.

B. Upper limits on the r-mode amplitude

The r-mode saturation amplitude α that supports gravitational wave emission with a strain h_0 at a fre-

quency f from a source at a distance D is [37]:

$$\alpha = \sqrt{\frac{5}{8\pi}} \frac{c^5}{G} \frac{h_0}{(2\pi f)^3} \frac{D}{MR^3 \tilde{J}} \tag{16}$$

where $\tilde{J}$ is the dimensionless canonical angular momentum of the r-mode [4]. $\tilde{J}$ is less dependant on the equation of state than M and R so, following [4], we fix its value to 0.0164 (as computed from a polytropic EoS with index $n = 1$) and encapsulate the dependancy on the equation of state in the term MR^3, as function of A.

The gravitational wave frequency also depends on A: $f = A\nu$. As done is Section V A 2 we consider

$$\begin{cases} \alpha^{\min}(h_0, A, f = A\nu_{\max}) = \sqrt{\frac{5}{8\pi}} \frac{c^5}{G} \frac{h_0}{(2\pi A\nu_{\max})^3} \frac{D}{M(A)R(A)^3\tilde{J}} \\ \alpha^{\max}(h_0, A, f = A\nu_{\min}) = \sqrt{\frac{5}{8\pi}} \frac{c^5}{G} \frac{h_0}{(2\pi A\nu_{\min})^3} \frac{D}{M(A)R(A)^3\tilde{J}} \end{cases} \tag{17}$$

and for each of these curves the range $A \in [1.39, 1.57]$ determines the range of variability of the saturation amplitude α as a function of h_0. In practice since $\alpha^{\min}(h_0, A, f = A\nu_{\max}) \approx \alpha^{\max}(h_0, A, f = A\nu_{\min})$ we convert the gravitational wave amplitude upper-limits $h_0^{90\%}$ to ranges for the r-mode amplitude upper limits in every half Hz bands as

$$\alpha^{90\%}(f) = \alpha(h_0^{90\%}, A, f = A\nu_{\min}), \ A \in [1.39, 1.57]. \tag{18}$$

The results are shown on Fig. (11) for all search runs. The shaded area represent the spread of α in the possible range of $M(A)R(A)^3$ bounded by realistic equations of state, as well as the upper limit for $M = 1.4\,M_\odot$, $R = 11.7$ km (middle black curve).

C. Not always "ON" signal

Our upper limits are based on the optimistic assumption that the r-mode signal is always "ON" during the time of the searches. This might not be the case because in the model that we consider, r-mode emission begins some time after a glitch and ends with the next glitch. Not knowing when glitches happened for J0537-6910 around the O1 and O2 observing times, we cannot be sure that some of our search times do not fall in a period too close to a glitch to be emitting r-modes, according to our model. In order to estimate the impact of this assumption we randomly pick start times for the O1 and O2 runs during the 13 years for which we have glitch-occurrence times and based on this glitch-time information, we compute the fraction of these simulated O1, O2.1 and O2.2 runs which overlaps with the r-mode emission period[38]. The resulting distributions for 1000 draws of the start times are shown in the top panel of Fig. 12. Since the data has gaps which are not uniformly distributed, the fraction of the overlapping *time* is not equal to the fraction of *data* in the overlap stretches, so we also compute this and show the distributions in the bottom panel of Fig. 12. We find that the 50th percentiles for the overlap fraction of the data are $\approx 45\%$ for O1 and $\approx 50\%$ for O2.1 and O2.2. We repeat the simulation-and-search Monte Carlos described in Section V A for O1, O2.2 and O2.2 with signals from this population and with frequency between 87.75 Hz and 88.25 Hz. In this sample frequency band we find a $h_0^{90\%}$ higher by a factor $\approx 4.4, 3.7$ and 4.2 respectively for the three searches, compared to the always-ON-signal results.

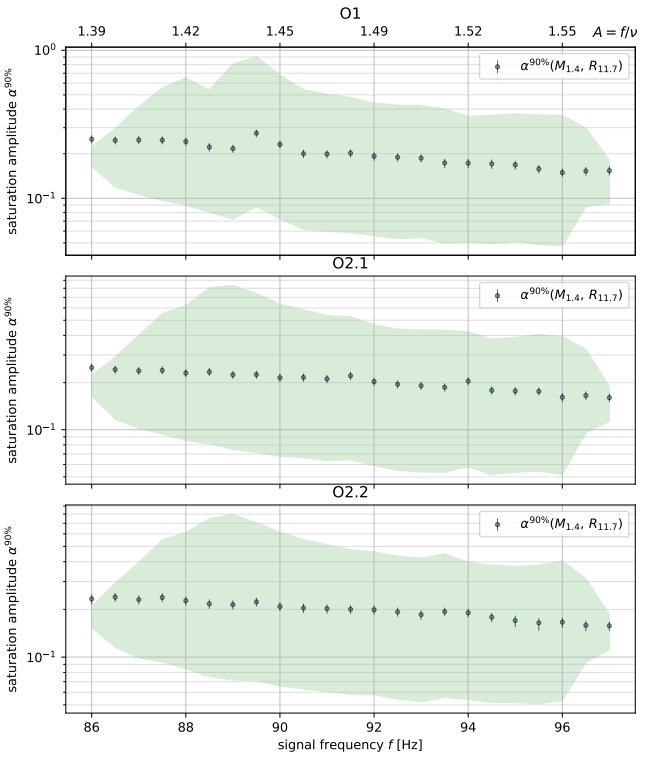

FIG. 11: Upper limits on the r-mode saturation amplitude α derived from the gravitational wave amplitude upper limits $h_0^{90\%}$.

VI. CONCLUSIONS

Pulsar J0537-6910 is an intriguiging candidate for r-mode gravitational wave emission $\gtrsim 50$ days after a glitch. Unfortunately we do not know whether the object glitched during the O1 and O2 LIGO data runs, so we carry out three coherent searches for r-mode continuous gravitational waves on periods lasting several tens of days. We choose the periods based on the available data and its gaps. We pick the frequency and frequency-derivative range to be large enough to include all uncertainties in the rotation frequency timing model, evolved to the time of the observations, and the uncertainties stemming from the unknown equation of state of the star.

This is the first search specifically targeting r-mode emission from a known pulsar. While we do not find

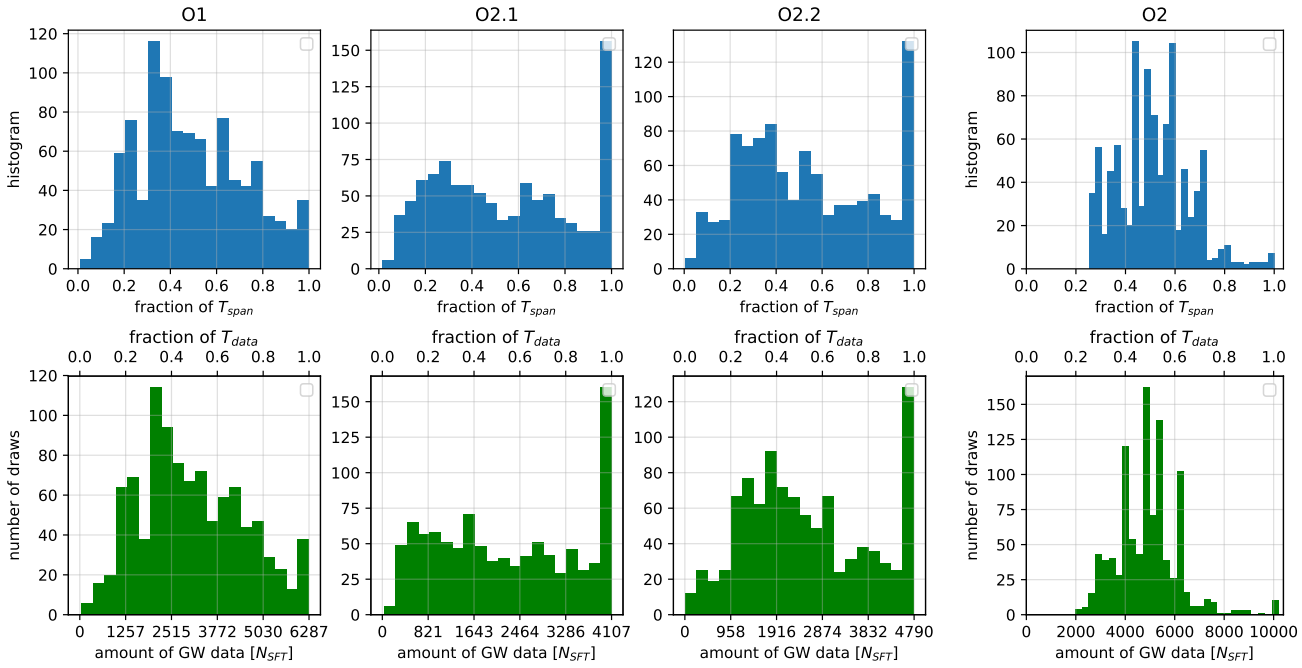

FIG. 12: Distributions of the fraction of the searches' observation spans $T_{\rm span}$ (top panels) and distribution of the amount of gravitational wave data $T_{\rm data}$ (lower panels) that overlap with unstable r-mode emission periods (for O1, O2.1 and O2.2) and that overlaps with the longest glitch-free period (for O2). The amount of data is expressed by the number of input SFTs ($N_{\rm SFT}$). The total number of SFTs is given in Tab. IV as $T_{\rm data}$ for O1, O2.1, O2.2, and $T_{\rm data} = 10194\,N_{\rm SFT}$ for O2. These r-mode emission periods are simulated by drawing 1000 random search start-times during the 13 years for which we have the occurrence-time of J0537-6910 glitches.

evidence for a continuous gravitational wave signal, we set upper limits on the gravitational wave amplitude of r-mode signals in 0.5 Hz bands. Overall the upper limits span a range between $(1.0-1.45)\times10^{-25}$, with an average sensitivity depth of ≈ 87 and 74 $\frac{1}{\sqrt{\rm Hz}}$ for the O1 and O2 searches respectively, consistent with the size of the data sets employed. The r-mode saturation amplitude values that this search could detect are consistent with those necessary to interpret the EM observations in terms of unstable r-mode emission [11]. They are about an order of magnitude larger than the physically most plausible ones but scenarios can be imagined where even such high values are possible. We refer the reader to the discussion on this point in Section 3 of [11]. Our upper limits are a factor of ≈ 5 higher than the average spin-down limit amplitude.

Lacking precise ephemeris data for this pulsar, J0537-6910 was not included in the LIGO 220+ known-pulsars search [39], but was later targeted in a small, 0.25 Hz search around twice the rotation frequency, 123.86 Hz, in [40]. That search, carried out on the O2 data, is limited to a spin-down range of 8×10^{-13} Hz/s and overall comprises $\sim 1.6\times10^{9}$ templates, about 10000 times fewer than employed here for each of our searches. The upper limits of [40] are consistent with the longer coherent time-baseline, the different level of the detector noise and the significantly smaller template bank of that search with respect to the one presented here.

As in [40], our upper limits are based on the optimistic assumption that the r-mode signal is always "ON" during the time of the searches. Based on historical glitch-occurrence times we construct a population of signals with varying durations and overlaps with our data-sets, and evaluate the upper-limits on this population of signals. The sensitivity is degraded with respect to the always-ON population by a factor ≈ 4.

The likelihood of a glitch occurring during the 232 days observation time of the LIGO search [40], is even higher, reflected in a mean overlap of the observation time with the longest inter-glitch periods of 50% (see Fig. 12). [40] do not comment on their loss of sensitivity due to a possible glitch of J0537-6910. We estimate that for a realistically glitching signal the upper limit $h_0^{95\%}$ of [40] would be ≈ 3.6 times higher, comparable to the degradation that we report for our searches. Timing of J0537-6910 in order to identify the times when glitches occur, eliminates all these uncertainties and is of paramount importance to search for continuous gravitational waves from J0537-6910.

A very interesting candidate from this search would be a high-significance signal consistent in at least two of the three searches. This would indicate a repeating phe-

nomenon exciting the star's r-mode instability, coherent with the observations of [11]. A definitive confirmation would need a verification on a different gravitational wave data set, corroborated by glitch information from EM observations. This re-inforces the importance of EM timing of J0537-6910.

A detection would be of great importance for multiple reasons. It would be i) the first detection of a continuous gravitational wave signal, opening interesting prospects for high-precision tests of gravity ii) the first direct observation of gravitational waves emission through unstable r-modes, as predicted in [2] iii) the discovery that at least some young neutron stars loose angular momentum due to r-mode gravitational waves iv) a probe of neutron star interior.

As new and more sensitive gravitational wave data becomes available, deeper searches will be possible, also including the use of specific techniques on longer data sets [41–43]. The scientific return of gravitational wave searches like this is greatly enhanced when timing data is available, that identifies the rotation parameters during the gravitational wave observations and glitch-occurrence times. NICER [1] could provide this invaluable information to the broad scientific community.

VII. ACKNOWLEDGMENTS

We thank Wynn Ho for useful discussions in the early phases of this project, Danai Antonopoulou for having supplied us with the numerical values of Table 1 and 2 of [10], Benjamin Steltner for having prepared the input data for this search, and Heinz-Bernd Eggenstein and the Einstein@Home team for access to the all-sky search results. We acknowledge David Keitel for his comments at our presentation at the 30th Texas Symposium in Portsmouth. A special thank-you to Nils Andersson for the many interesting discussions and for his comments on the manuscript.
This research has made use of data and web tools for data transfer of the Gravitational Wave Open Science Center [44], a service of LIGO Laboratory, the LIGO Scientific Collaboration and the Virgo Collaboration. LIGO is funded by the U.S. National Science Foundation. Virgo is funded by the French Centre National de Recherche Scientifique (CNRS), the Italian Istituto Nazionale della Fisica Nucleare (INFN) and the Dutch Nikhef, with contributions by Polish and Hungarian institutes.

[1] NICER, "The neutron star interior composition explorer mission," (2017), https://heasarc.gsfc.nasa.gov/docs/nicer/.
[2] N. Andersson, "A New class of unstable modes of rotating relativistic stars," (1998), arXiv:gr-qc/9706075 [gr-qc].
[3] J. L. Friedman and S. M. Morsink, "Axial instability of rotating relativistic stars," (1998), arXiv:gr-qc/9706073 [gr-qc].
[4] B. J. Owen, L. Lindblom, C. Cutler, B. F. Schutz, A. Vecchio, and N. Andersson, "Gravitational waves from hot young rapidly rotating neutron stars," (1998), arXiv:gr-qc/9804044 [gr-qc].
[5] L. Lindblom, B. J. Owen, and S. M. Morsink, "Gravitational radiation instability in hot young neutron stars," (1998), arXiv:gr-qc/9803053 [gr-qc].
[6] N. Andersson, K. D. Kokkotas, and B. F. Schutz, "Gravitational radiation limit on the spin of young neutron stars," (1999), arXiv:astro-ph/9805225 [astro-ph].
[7] F. E. Marshall, E. V. Gotthelf, W. Zhang, J. Middleditch, and Q. D. Wang, "Discovery of an ultra-fast x-ray pulsar in the supernova remnant n157b," (1998), arXiv:astro-ph/9803214 [astro-ph].
[8] R. N. Manchester, G. B. Hobbs, A. Teoh, and M. Hobbs, "The Australia Telescope National Facility pulsar catalogue," (2005), arXiv:astro-ph/0412641 [astro-ph].
[9] M. G. Alford and K. Schwenzer, "Gravitational wave emission and spindown of young pulsars," (2014), arXiv:1210.6091 [gr-qc].
[10] D. Antonopoulou, C. M. Espinoza, L. Kuiper, and N. Andersson, "Pulsar spin-down: the glitch-dominated rotation of PSR J0537-6910," (2018), arXiv:1708.09459 [astro-ph.HE].
[11] N. Andersson, D. Antonopoulou, C. M. Espinoza, B. Haskell, and W. C. G. Ho, "The Enigmatic Spin Evolution of PSR J0537-6910: r-modes, Gravitational Waves, and the Case for Continued Timing," (2018), arXiv:1711.05550 [astro-ph.HE].
[12] M. Vallisneri, J. Kanner, R. Williams, A. Weinstein, and B. Stephens, "The LIGO open science center," (2015).
[13] LIGO, "The o1 data release," (2018), https://www.gw-openscience.org/O1/.
[14] LIGO, "The o2 data release," (2018), https://www.gw-openscience.org/O2/.
[15] S. Caride, R. Inta, B. J. Owen, and B. Rajbhandari, "How to search for gravitational waves from r-modes of known pulsars," (2019), arXiv:1907.04946 [gr-qc].
[16] B. P. Abbott et al. (LIGO Scientific), "LIGO: The Laser interferometer gravitational-wave observatory," (2009), arXiv:0711.3041 [gr-qc].
[17] B. P. Abbott et al. (LIGO Scientific, Virgo), "GW150914: The Advanced LIGO Detectors in the Era of First Discoveries," (2016), arXiv:1602.03838 [gr-qc].
[18] J. Aasi et al. (LIGO Scientific), "Advanced LIGO," (2015), arXiv:1411.4547 [gr-qc].
[19] B. P. Abbott et al. (LIGO Scientific, Virgo), "GWTC-1: A Gravitational-Wave Transient Catalog of Compact Binary Mergers Observed by LIGO and Virgo during the First and Second Observing Runs," (2019), arXiv:1811.12907 [astro-ph.HE].
[20] LIGO, "O2 summary," (2018), https://www.gw-openscience.org/summary_pages/detector_status/O2/.
[21] B. Allen and G. Mendell, "Sft data format version 2 specification," (2004).

[22] P. B. Covas et al. (LSC), "Identification and mitigation of narrow spectral artifacts that degrade searches for persistent gravitational waves in the first two observing runs of Advanced LIGO," (2018), arXiv:1801.07204 [astro-ph.IM].

[23] B. P. Abbott et al. (LIGO Scientific, Virgo), "First low-frequency Einstein@Home all-sky search for continuous gravitational waves in Advanced LIGO data," (2017), arXiv:1707.02669 [gr-qc].

[24] P. Jaranowski, A. Krolak, and B. F. Schutz, "Data analysis of gravitational - wave signals from spinning neutron stars. 1. The Signal and its detection," (1998), arXiv:gr-qc/9804014 [gr-qc].

[25] C. Cutler and B. F. Schutz, "The Generalized F-statistic: Multiple detectors and multiple GW pulsars," (2005), arXiv:gr-qc/0504011 [gr-qc].

[26] D. Keitel, R. Prix, M. A. Papa, P. Leaci, and M. Siddiqi, "Search for continuous gravitational waves: Improving robustness versus instrumental artifacts," (2014), arXiv:1311.5738 [gr-qc].

[27] B. Behnke, M. A. Papa, and R. Prix, "Post-processing methods used in the search for continuous gravitational-wave signals from the Galactic Center," (2015), arXiv:1410.5997 [gr-qc].

[28] Python, "Curve fitting documentation," (2019).

[29] C. Cahillane et al. (LIGO Scientific), "Calibration uncertainty for Advanced LIGOs first and second observing runs," (2017), arXiv:1708.03023 [astro-ph.IM].

[30] AEI, "Supplementary material for the publication," (2020), available at `https://www.aei.mpg.de/continuouswaves/j0537`.

[31] C. Dreissigacker, R. Prix, and K. Wette, "Fast and Accurate Sensitivity Estimation for Continuous-Gravitational-Wave Searches," (2018), arXiv:1808.02459 [gr-qc].

[32] J. Aasi et al. (LIGO Scientific), "Gravitational waves from known pulsars: results from the initial detector era," (2014), arXiv:1309.4027 [astro-ph.HE].

[33] A. Idrisy, B. J. Owen, and D. I. Jones, "R-mode frequencies of slowly rotating relativistic neutron stars with realistic equations of state," (2015), arXiv:1410.7360 [gr-qc].

[34] F. Ozel, D. Psaltis, T. Guver, G. Baym, C. Heinke, and S. Guillot, "The Dense Matter Equation of State from Neutron Star Radius and Mass Measurements," (2016), arXiv:1505.05155 [astro-ph.HE].

[35] F. Ozel, D. Psaltis, T. Guver, G. Baym, C. Heinke, and S. Guillot, "Neutron stars tabulated equations of state," (2016), `http://xtreme.as.arizona.edu/NeutronStars/`.

[36] C. Breu and L. Rezzolla, "Maximum mass, moment of inertia and compactness of relativistic stars," (2016), arXiv:1601.06083 [gr-qc].

[37] B. J. Owen, "How to adapt broad-band gravitational-wave searches for r-modes," (2010), arXiv:1006.1994 [gr-qc].

[38] We recall that we have defined the r-mode emission period to be the period 50-day after a glitch to the next glitch..

[39] B. P. Abbott et al. (LIGO Scientific, Virgo), "Searches for Gravitational Waves from Known Pulsars at Two Harmonics in 2015-2017 LIGO Data," (2019), arXiv:1902.08507 [astro-ph.HE].

[40] B. P. Abbott et al. (LIGO Scientific, Virgo), "Narrow-band search for gravitational waves from known pulsars using the second LIGO observing run," (2019), arXiv:1902.08442 [gr-qc].

[41] D. Keitel, "Robust semicoherent searches for continuous gravitational waves with noise and signal models including hours to days long transients," (2016), arXiv:1509.02398 [gr-qc].

[42] D. Keitel and G. Ashton, "Faster search for long gravitational-wave transients: GPU implementation of the transient $\mathcal{F}$-statistic," (2018), arXiv:1805.05652 [astro-ph.IM].

[43] G. Ashton, R. Prix, and D. I. Jones, "A semicoherent glitch-robust continuous-gravitational-wave search method," (2018), arXiv:1805.03314 [gr-qc].

[44] LIGO, "Ligo open science center," (2018), `https://www.gw-openscience.org/`.

Appendix A: Excluded frequency bands

Search run	O1	
central f [Hz]	$-\Delta f$ [Hz]	$+\Delta f$ [Hz]
Hanford (LHO)		
86.0000000	0.0065	0.0020
86.5000000	0.0065	0.0020
87.0000000	0.0065	0.0020
87.5000000	0.0065	0.0020
88.0000000	0.0060	0.0015
88.0000000	0.0065	0.0020
88.5000000	0.0065	0.0020
89.0000000	0.0065	0.0020
89.5000000	0.0065	0.0020
90.0000000	0.0065	0.0020
90.5000000	0.0065	0.0020
91.0000000	0.0065	0.0020
91.5000000	0.0065	0.0020
92.0000000	0.0065	0.0020
92.5000000	0.0065	0.0020
93.0000000	0.0065	0.0020
93.5000000	0.0065	0.0020
94.0000000	0.0065	0.0020
94.2381000	0.0085	0.0040
94.2447000	0.0085	0.0040
94.5000000	0.0065	0.0020
95.0000000	0.0065	0.0020
95.5000000	0.0065	0.0020
96.0000000	0.0060	0.0015
96.0000000	0.0065	0.0020
96.5000000	0.0065	0.0020
97.0000000	0.0065	0.0020
Livingston (LLO)		
86.7497500	0.0065	0.0020
87.7497250	0.0065	0.0020
87.9000000	0.0060	0.0015
88.4000000	0.0060	0.0015
88.7497000	0.0065	0.0020
89.7496750	0.0065	0.0020
90.3000000	0.0060	0.0015
90.7496500	0.0065	0.0020
90.8000000	0.0060	0.0015
91.3000000	0.0060	0.0015
91.7496250	0.0065	0.0020
92.7496000	0.0065	0.0020
93.7000000	0.0060	0.0015
93.7495750	0.0065	0.0020
94.2000000	0.0060	0.0015
94.7495500	0.0065	0.0020
95.7495250	0.0065	0.0020
95.8831600	0.0119	0.0042
96.6000000	0.0060	0.0015
96.7495000	0.0065	0.0020
97.1000000	0.0060	0.0015

TABLE VI: Excluded frequency bands in O1 search run

Search run	O2.1		O2.2	
central f [Hz]	$-\Delta f$ [Hz]	$+\Delta f$ [Hz]	$-\Delta f$ [Hz]	$+\Delta f$ [Hz]
Hanford (LHO)				
85.9987000	0.0004	0.0011	0.0039	0.0065
86.0000000	0.0004	0.0011	0.0039	0.0065
86.5000000	0.0023	0.0030	0.0058	0.0083
86.7498371	0.0004	0.0011	0.0039	0.0065
86.9987000	0.0004	0.0011	0.0039	0.0065
87.0000000	0.0004	0.0011	0.0039	0.0065
87.5000000	0.0023	0.0030	0.0058	0.0083
87.7498217	0.0004	0.0011	0.0039	0.0065
87.9987000	0.0004	0.0011	0.0039	0.0065
88.0000000	0.0004	0.0011	0.0039	0.0065
88.5000000	0.0023	0.0030	0.0058	0.0083
88.7498063	0.0004	0.0011	0.0039	0.0065
88.8894000	0.0004	0.0011	0.0039	0.0065
88.8898400	0.0004	0.0011	0.0039	0.0065
88.9987000	0.0004	0.0011	0.0039	0.0065
89.0000000	0.0004	0.0011	0.0039	0.0065
89.5000000	0.0023	0.0030	0.0058	0.0083
89.7497909	0.0004	0.0011	0.0039	0.0065
89.9987000	0.0004	0.0011	0.0039	0.0065
90.0000000	0.0004	0.0011	0.0039	0.0065
90.5000000	0.0023	0.0030	0.0058	0.0083
90.7497755	0.0004	0.0011	0.0039	0.0065
90.9987000	0.0004	0.0011	0.0039	0.0065
91.0000000	0.0004	0.0011	0.0039	0.0065
91.1602520	0.0043	0.0050	0.0077	0.0103
91.5000000	0.0023	0.0030	0.0058	0.0083
91.7497601	0.0004	0.0011	0.0039	0.0065
91.9987000	0.0004	0.0011	0.0039	0.0065
92.0000000	0.0004	0.0011	0.0039	0.0065
92.5000000	0.0023	0.0030	0.0058	0.0083
92.7497447	0.0004	0.0011	0.0039	0.0065
92.9987000	0.0004	0.0011	0.0039	0.0065
93.0000000	0.0004	0.0011	0.0039	0.0065
93.5000000	0.0023	0.0030	0.0058	0.0083
93.7497293	0.0004	0.0011	0.0039	0.0065
93.9987000	0.0004	0.0011	0.0039	0.0065
94.0000000	0.0004	0.0011	0.0039	0.0065
94.5000000	0.0023	0.0030	0.0058	0.0083
94.7497139	0.0004	0.0011	0.0039	0.0065
94.9987000	0.0004	0.0011	0.0039	0.0065
95.0000000	0.0004	0.0011	0.0039	0.0065
95.5000000	0.0023	0.0030	0.0058	0.0083
95.7496985	0.0004	0.0011	0.0039	0.0065
95.9987000	0.0004	0.0011	0.0039	0.0065
96.0000000	0.0004	0.0011	0.0039	0.0065
96.5000000	0.0023	0.0030	0.0058	0.0083
96.7496831	0.0004	0.0011	0.0039	0.0065
96.9987000	0.0004	0.0011	0.0039	0.0065
97.0000000	0.0004	0.0011	0.0039	0.0065

Search run	O2.1		O2.2	
central f [Hz]	$-\Delta f$ [Hz]	$+\Delta f$ [Hz]	$-\Delta f$ [Hz]	$+\Delta f$ [Hz]
Livingston (LLO)				
86.0000000	0.0004	0.0011	0.0039	0.0065
86.7206543	0.0006	0.0013	0.0040	0.0066
86.7211041	0.0004	0.0011	0.0039	0.0065
87.0000000	0.0004	0.0011	0.0039	0.0065
87.7174434	0.0006	0.0013	0.0040	0.0066
87.7178984	0.0004	0.0011	0.0039	0.0065
88.0000000	0.0004	0.0011	0.0039	0.0065
88.7142326	0.0006	0.0013	0.0040	0.0066
88.7146927	0.0004	0.0011	0.0039	0.0065
89.0000000	0.0004	0.0011	0.0039	0.0065
89.7110217	0.0006	0.0013	0.0040	0.0066
89.7114870	0.0004	0.0011	0.0039	0.0065
90.0000000	0.0004	0.0011	0.0039	0.0065
90.7078108	0.0006	0.0013	0.0040	0.0066
90.7082813	0.0004	0.0011	0.0039	0.0065
91.0000000	0.0004	0.0011	0.0039	0.0065
91.7046000	0.0006	0.0013	0.0040	0.0066
91.7050756	0.0004	0.0011	0.0039	0.0065
92.0000000	0.0004	0.0011	0.0039	0.0065
92.7013891	0.0006	0.0013	0.0040	0.0066
92.7018699	0.0004	0.0011	0.0039	0.0065
93.0000000	0.0004	0.0011	0.0039	0.0065
93.6981782	0.0006	0.0013	0.0040	0.0066
93.6986642	0.0004	0.0011	0.0039	0.0065
94.0000000	0.0004	0.0011	0.0039	0.0065
94.6949673	0.0006	0.0013	0.0040	0.0066
94.6954585	0.0004	0.0011	0.0039	0.0065
95.0000000	0.0004	0.0011	0.0039	0.0065
95.6917565	0.0006	0.0013	0.0040	0.0066
95.6922528	0.0004	0.0011	0.0039	0.0065
96.0000000	0.0004	0.0011	0.0039	0.0065
96.6885456	0.0006	0.0013	0.0040	0.0066
96.6890471	0.0004	0.0011	0.0039	0.0065
97.0000000	0.0004	0.0011	0.0039	0.0065

TABLE VII: Excluded frequency bands in O2.1 and O2.2 search runs

Appendix B: Upper limits on GW and saturation amplitude

$f_{\rm GW}$ ± 0.25 [Hz]	$h_{0\ \rm min}^{\rm sd}$ $[10^{-26}]$	$h_{0\ \rm max}^{\rm sd}$ $[10^{-26}]$
86.0	1.36	2.30
86.5	1.21	2.59
87.0	1.10	2.78
87.5	1.01	2.96
88.0	0.96	3.07
88.5	1.02	3.20
89.0	0.88	3.30
89.5	0.93	3.39
90.0	0.98	3.45
90.5	1.02	3.51
91.0	1.06	3.57
91.5	1.09	3.63
92.0	1.11	3.65
92.5	1.13	3.74
93.0	1.13	3.76
93.5	1.13	3.75
94.0	1.19	3.79
94.5	1.18	3.78
95.0	1.17	3.73
95.5	1.16	3.73
96.0	1.14	3.70
96.5	1.24	2.97
97.0	1.51	2.77

TABLE VIII: Spindown limits $h_0^{\rm sd}$ for each 0.5 Hz over the entire search range.

$h_0^{90\%}$ $[10^{-25}]$	$\alpha^{90\%}$	$\sqrt{S_h}$ $[10^{-23}]$ $[1/\sqrt{\rm Hz}]$	$\mathcal{D}^{90\%}$ $[1/\sqrt{\rm Hz}]$
$1.16^{+0.015}_{-0.015}$	0.25	1.01	87.2
$1.16^{+0.013}_{-0.014}$	0.25	1.04	89.3
$1.19^{+0.013}_{-0.014}$	0.25	1.10	92.0
$1.21^{+0.016}_{-0.016}$	0.25	1.07	88.5
$1.20^{+0.015}_{-0.015}$	0.24	1.01	84.0
$1.12^{+0.015}_{-0.015}$	0.22	0.98	87.8
$1.11^{+0.013}_{-0.015}$	0.22	0.97	87.0
$1.44^{+0.013}_{-0.014}$	0.28	0.98	68.3
$1.23^{+0.012}_{-0.012}$	0.23	0.96	77.7
$1.08^{+0.013}_{-0.015}$	0.20	0.95	87.8
$1.09^{+0.013}_{-0.015}$	0.20	0.95	87.3
$1.13^{+0.014}_{-0.014}$	0.20	0.96	84.8
$1.09^{+0.014}_{-0.016}$	0.19	0.95	87.1
$1.09^{+0.013}_{-0.017}$	0.19	0.94	86.2
$1.10^{+0.013}_{-0.016}$	0.19	0.93	84.8
$1.03^{+0.017}_{-0.026}$	0.17	0.92	89.1
$1.05^{+0.016}_{-0.024}$	0.17	0.91	87.0
$1.05^{+0.017}_{-0.025}$	0.17	0.90	85.5
$1.05^{+0.013}_{-0.017}$	0.17	0.89	84.7
$1.00^{+0.014}_{-0.016}$	0.16	0.89	88.2
$0.96^{+0.011}_{-0.013}$	0.16	0.88	91.0
$1.00^{+0.013}_{-0.018}$	0.15	0.87	87.0
$1.03^{+0.022}_{-0.022}$	0.15	0.87	85.0

TABLE IX: Upper limits for O1 search run.

$h_0^{90\%}$ $[10^{-25}]$	$\alpha^{90\%}$	$\sqrt{S_h}$ $[10^{-23}]$ $[1/\sqrt{\rm Hz}]$	$\mathcal{D}^{90\%}$ $[1/\sqrt{\rm Hz}]$
$1.16^{+0.010}_{-0.011}$	0.25	0.87	75.2
$1.15^{+0.008}_{-0.009}$	0.24	0.86	75.1
$1.15^{+0.008}_{-0.008}$	0.24	0.86	74.8
$1.17^{+0.010}_{-0.010}$	0.24	0.86	73.5
$1.15^{+0.009}_{-0.011}$	0.23	0.86	74.9
$1.19^{+0.009}_{-0.010}$	0.23	0.85	71.9
$1.16^{+0.008}_{-0.009}$	0.22	0.85	73.7
$1.18^{+0.009}_{-0.010}$	0.22	0.86	73.0
$1.15^{+0.009}_{-0.009}$	0.21	0.85	74.5
$1.17^{+0.010}_{-0.010}$	0.22	0.85	72.4
$1.16^{+0.010}_{-0.011}$	0.21	0.85	73.4
$1.24^{+0.011}_{-0.012}$	0.22	0.86	69.7
$1.15^{+0.009}_{-0.008}$	0.20	0.86	74.6
$1.13^{+0.009}_{-0.009}$	0.20	0.85	75.7
$1.12^{+0.010}_{-0.011}$	0.19	0.85	75.6
$1.11^{+0.010}_{-0.010}$	0.19	0.85	76.0
$1.24^{+0.010}_{-0.010}$	0.20	0.84	67.7
$1.10^{+0.010}_{-0.010}$	0.18	0.83	75.3
$1.11^{+0.010}_{-0.011}$	0.18	0.82	73.6
$1.12^{+0.008}_{-0.010}$	0.18	0.81	72.1
$1.04^{+0.012}_{-0.015}$	0.16	0.80	76.8
$1.09^{+0.011}_{-0.013}$	0.17	0.80	73.4
$1.07^{+0.012}_{-0.015}$	0.16	0.80	74.4

TABLE X: Upper limits for O2.1 search run.

$h_0^{90\%}$ $[10^{-25}]$	$\alpha^{90\%}$	$\sqrt{S_h}$ $[10^{-23}]$ $[1/\sqrt{\rm Hz}]$	$\mathcal{D}^{90\%}$ $[1/\sqrt{\rm Hz}]$
$1.08^{+0.019}_{-0.029}$	0.23	0.82	76.1
$1.13^{+0.012}_{-0.014}$	0.24	0.82	72.5
$1.11^{+0.014}_{-0.019}$	0.23	0.82	74.2
$1.16^{+0.015}_{-0.016}$	0.24	0.83	71.4
$1.13^{+0.014}_{-0.017}$	0.23	0.84	73.8
$1.10^{+0.015}_{-0.022}$	0.22	0.83	75.2
$1.10^{+0.015}_{-0.019}$	0.21	0.83	74.9
$1.17^{+0.014}_{-0.016}$	0.22	0.83	70.7
$1.11^{+0.014}_{-0.018}$	0.21	0.83	74.4
$1.11^{+0.016}_{-0.021}$	0.20	0.82	74.2
$1.11^{+0.014}_{-0.019}$	0.20	0.82	73.8
$1.12^{+0.012}_{-0.015}$	0.20	0.83	73.9
$1.13^{+0.014}_{-0.017}$	0.20	0.83	73.1
$1.12^{+0.015}_{-0.020}$	0.19	0.82	73.4
$1.09^{+0.014}_{-0.021}$	0.19	0.82	75.5
$1.16^{+0.010}_{-0.012}$	0.19	0.86	74.1
$1.16^{+0.012}_{-0.015}$	0.19	0.85	73.5
$1.10^{+0.016}_{-0.023}$	0.18	0.80	72.9
$1.07^{+0.022}_{-0.040}$	0.17	0.79	73.8
$1.05^{+0.020}_{-0.058}$	0.16	0.78	74.4
$1.07^{+0.017}_{-0.029}$	0.17	0.77	72.1
$1.04^{+0.017}_{-0.033}$	0.16	0.77	74.0
$1.05^{+0.014}_{-0.025}$	0.16	0.77	73.5

TABLE XI: Upper limits for O2.2 search run.

We stress that the $h_0^{90\%}$ and $\alpha^{90\%}$ upper limits do not hold in the sub-bands of Table A.